RSC Advances

PAPER

View Article Online
View Journal | View Issue

Cite this: *RSC Adv.*, 2026, **16**, 24454

Synthesis of La-Fe_3O_4@polydopamine core–shell magnetic composites for enhanced phosphate removal from aqueous solutions

Xinyu Cheng,†[ab] Zhihua Xu,†[ac] Chenxi Guo,[a] Ting Zhou,[ac] Alang Zhang[a] and Feng Shi *[a]

Received 27th January 2026
Accepted 28th April 2026

DOI: 10.1039/d6ra00725b

rsc.li/rsc-advances

In this work, a lanthanum-doped Fe_3O_4@polydopamine (PDA) core–shell composite was prepared *via* a hydrothermal method. XPS depth profiling revealed that La is uniformly distributed throughout the Fe_3O_4 particles, with a constant La/Fe ratio from the surface to 60 nm depth. The material exhibits superparamagnetic properties, enabling rapid magnetic separation within 30 s. Phosphate adsorption reaches equilibrium in 180 min, following pseudo-second-order kinetics (R^2 > 0.999) and the Sips isotherm, with a maximum capacity of 123.44 mg P per g. XPS analysis revealed shifts in the La 3d spectra consistent with inner-sphere La–P complexation, providing supportive evidence for chemisorption. The adsorbent retained >85% of its capacity after five cycles using 1 M NaCl as the eluent. Negligible La leaching (<0.01 μg L^{-1}) and low aquatic toxicity to *Chlorella* sp. further support its environmental safety. These results demonstrate that 2.5%La-Fe_3O_4@PDA provides a robust, magnetically separable, and reusable platform for phosphate removal, offering deeper mechanistic insights into La-doping and PDA synergy in established magnetic core–shell systems.

Introduction

Phosphorus (P) is an indispensable nutrient for the growth and reproduction of all organisms.[1] However, the excessive discharge of phosphate into water bodies from agricultural runoff and domestic/industrial wastewater has emerged as one of the most pressing global environmental challenges of the 21st century. This leads to eutrophication, characterized by harmful algal blooms, reduced water transparency, and dissolved oxygen depletion, ultimately causing the collapse of ecosystem functions and a loss of biodiversity.[2]

Phosphate removal employs various technologies,[3] including chemical precipitation,[4] biological treatment,[5] membrane filtration,[6] and adsorption.[7,8] Among these, adsorption is widely regarded as one of the most promising methods due to its simplicity, cost-effectiveness, high efficiency, and potential for phosphate recovery.[3] Nanomaterial adsorbents have demonstrated exceptional pollutant removal capabilities in the field of water treatment owing to their ultra-high specific surface area and reactivity, such as layered double hydroxides (LDHs),[9] metal–organic frameworks (MOFs),[10] biochar,[8] and hydrogels.[11] However, it is the high dispersion and low sedimentation brought about by its nanoscale size (<100 nm) that cause it to face inherent defects, such as difficulties in separation and recycling, a surge in operating costs, and potential secondary ecological risks in practical applications.

To overcome this bottleneck, superparamagnetic adsorbents have emerged as a promising solution. These materials typically use superparamagnetic nanoparticles (such as Fe_3O_4) as the magnetic core, allowing the adsorbents to be rapidly and efficiently separated from water using an external magnetic field after adsorption. This avoids the filtration difficulties associated with conventional powdered adsorbents and greatly facilitates the regeneration and recycling of the adsorbents.[12–14] Despite the obvious advantages, pure Fe_3O_4 nanoparticles also have the disadvantage of being easily oxidized and aggregated in aqueous solutions, which reduces their adsorption efficiency and long-term stability.[15–17] Therefore, by surface modification[18–20] or composite techniques,[21,22] functional groups or porous materials with specific adsorption capabilities can be combined on the Fe_3O_4 magnetic core, achieving both high adsorption performance and convenient magnetic-responsive separation, which is key to enhancing their practical application performance.

Among them, the rare earth element lantanth (La) has a strong affinity for Lewis bases such as phosphate radicals (PO_4^{3-}) due to its unique electron layer structure and strong Lewis's acidity, which can form extremely stable lanthane phosphate ($LaPO_4$)[23,24] precipitation and is recognized as one of

[a]College of Life Sciences, Shihezi University, China. E-mail: shifeng2314@yeah.net
[b]Xinjiang Production and Construction Corps, Key Laboratory of Oasis Town and Mountain-basin System Ecology, China
[c]Key Laboratory of Xinjiang Phytomedicine Resource Utilization, Ministry of Education, China
† Equal contribution.

the most effective metals to capture phosphate. The effectiveness of this strategy has been widely confirmed by anchoring La on the magnetic carrier to construct an adsorbent with both high-efficiency adsorption and convenient separation characteristics. For instance, Wang *et al.*[25] fabricated a magnetic La–Fe co-loaded calcined soda residue *via* co-precipitation, achieving a phosphate adsorption capacity of 74.87 mg P per g. Despite these advances, significant hurdles persist for La-based magnetic adsorbents, including potential La leaching under acidic conditions and the gradual deactivation of active sites over repeated adsorption–desorption cycles.[26] Lu *et al.*[27] effectively prevented the oxidation of the magnetic nucleus by introducing a dense SiO_2 protective layer between its Fe_3O_4 magnetic nucleus and the $La(OH)_3$ active layer, successfully constructing a core–shell structural adsorbent with a high adsorption capacity (63.72 mg P per g) and excellent magnetic separation performance. However, such inorganic layers (*e.g.*, SiO_2) often lack sufficient surface functional groups, limiting further functionalization and the multifaceted tuning of adsorption properties. Polydopamine (PDA) stands out for its exceptional biocompatibility, environmental friendliness, and strong adhesive properties.[28] Its monomer dopamine can self-polymerize in a weakly alkaline aqueous solution to form a powerful coating layer on the surface of various materials.[29,30] This adhesion results from the strong coordination of catechol groups and metal oxides in dopamine molecules, ensuring the mechanical stability of the shell.[31] Rich functional groups provide a large number of phenol hydroxyl groups, amino groups, and other active sites, which not only serve as an ideal platform for subsequent modification but can also initially adsorb phosphate through hydrogen bonds and other interactions. In this study, we systematically investigate a La-doped Fe_3O_4@PDA core–shell composite to elucidate the synergistic role of bulk La incorporation and the PDA coating in enhancing phosphate adsorption, providing mechanistic validation and performance optimization of existing magnetic adsorbent strategies.

As the magnetic core, Fe_3O_4 magnetic nanoparticles are applied to various suitable fields depending on different preparation methods.[32] Bruckmann *et al.*[33] synthesized Fe_3O_4 by the co-precipitation method and coated a layer of chitosan (CS) on the basis of Fe_3O_4 as the core to prepare a magnetic composite (CS-Fe_3O_4). Magnetic nanoparticles uniformly covered with a polymer matrix can achieve efficient adsorption of tetracycline. Divakara *et al.*[34] reviewed the green synthesis of spinel ferrite nanoparticles and their nanocomposites, and discussed the applications of these green-synthesized materials in the fields of antibacterial activity, photocatalytic degradation of organic dyes, and wastewater treatment. Aboelfetoh[35] used the classical hydrothermal synthesis method to obtain Ag-doped reduced graphene oxide (rGO)-stabilized Fe_3O_4 composites (rGO/Fe_3O_4/Ag). The integration of rGO/Fe_3O_4/Ag enhanced the catalytic and adsorption capabilities of the nanomaterials, providing research progress for future environmental remediation applications. According to the purpose of this study, a La-doped spherical Fe_3O_4 magnetic core was prepared by a simple hydrothermal synthesis method. Subsequently, based on this, the polymerization characteristics of PDA were utilized to coat the surface, in order to obtain a novel integrated enhanced adsorbent.

In this work, a core–shell structured La-Fe_3O_4@PDA composite was synthesized *via* a hydrothermal method followed by PDA self-polymerization. The material was systematically characterized, and batch adsorption experiments were conducted to evaluate the effects of pH, adsorbent dosage, contact time, and initial concentration. Kinetic and isotherm models were applied to elucidate the adsorption mechanism, and the recyclability was assessed. The composite exhibits good superparamagnetism, selectivity, easy magnetic separation, and low environmental impact. This work advances the understanding of prior La-modified Fe_3O_4 and Fe_3O_4@PDA systems by providing XPS depth-profiling evidence of uniform La incorporation, spectroscopic data consistent with inner-sphere La–P interactions, and comprehensive environmental safety assessment. These features, together with the synergistic role of the PDA shell, validate 2.5%La-Fe_3O_4@PDA as a magnetically separable, reusable, and safe adsorbent with competitive phosphate capacity.

Materials and methods

Materials

Ferric chloride hexahydrate ($FeCl_3 \cdot 6H_2O$), sodium acetate (NaOAc), ethylenediaminetetraacetic acid disodium salt (EDTA-2Na), ethylene glycol (EG), dopamine hydrochloride, potassium dihydrogen phosphate (KH_2PO_4, AR, ≥99%), and ascorbic acid (AR, ≥99.7%) were purchased from Aladdin Biochemical Technology Co., Ltd. Potassium antimonyl tartrate (AR, ≥99%) and ammonium molybdate tetrahydrate ($(NH_4)_2MoO_4 \cdot 4H_2O$, AR, ≥99%) were also obtained from Aladdin. Lanthanum nitrate hexahydrate ($La(NO_3)_3 \cdot 6H_2O$, AR, ≥99%) and ethanol were supplied by Macklin Biochemical Technology Co., Ltd. *Chlorella* sp. was purchased from the Freshwater Algae Culture Collection, Institute of the Chinese Academy of Sciences. Deionized (DI) water was used throughout the experiments.

Hydrothermal synthesis of Fe_3O_4 nanoparticles

Fe_3O_4 nanoparticles were synthesized *via* a modified solvothermal method. In a typical procedure, $FeCl_3 \cdot 6H_2O$ (0.68 g), NaOAc (1.2 g), and EDTA-2Na (0.034 g) were dissolved in 20 mL of ethylene glycol under magnetic stirring for 1 h. The homogeneous yellow solution was then transferred into a 50 mL Teflon-lined stainless-steel autoclave and heated at 200 °C for 10 h. After cooling naturally to room temperature, the resulting black precipitate was collected magnetically and washed several times with anhydrous ethanol and DI water, followed by drying under vacuum at 60 °C for 12 h.

Hydrothermal synthesis of La-doped Fe_3O_4(La-Fe_3O_4)

The synthesis of La-Fe_3O_4 followed a similar procedure to that of pure Fe_3O_4, with the addition of a La precursor. Specifically, after the initial mixture of $FeCl_3 \cdot 6H_2O$ (0.68 g), NaOAc (1.2 g), and EDTA-2Na (0.034 g) in 20 mL ethylene glycol was stirred for

1 h, a predetermined volume of $La(NO_3)_3 \cdot 6H_2O$ solution (in ethylene glycol) was added dropwise under vigorous stirring to achieve a nominal La doping concentration. The mixture was stirred for an additional 30 min before being transferred to the autoclave for hydrothermal reaction (200 °C, 10 h). The final product was washed and dried using the same protocol as for the pure Fe_3O_4 nanoparticles described above.

Synthesis of La-Fe_3O_4@PDA core–shell nanoparticles

The La-Fe_3O_4@PDA composite was prepared *via* the *in situ* self-polymerization of dopamine on the surface of the as-synthesized La-Fe_3O_4 nanoparticles. First, La-Fe_3O_4 powder was dispersed in 50 mL of Tris–HCl buffer (10 mM, pH 8.5) by sonication for 5 min. Subsequently, 40 mg of dopamine hydrochloride was added to the suspension under mechanical stirring. The reaction was allowed to proceed at 30 °C for 24 h. The resulting black product, denoted as La-Fe_3O_4@PDA, was collected magnetically, thoroughly washed with ethanol and DI water, and finally freeze-dried for 12 h.

Characterization techniques

The crystal structure and phase composition of the synthesized samples were determined using X-ray diffraction (XRD, Rigaku SmartLab) with Cu Kα radiation ($\lambda = 1.5406$ Å) and a scanning 2θ range from 10° to 90°. Morphology and microstructure were examined by transmission electron microscopy (TEM, JEOL JEM-2100F). Elemental composition and mapping were performed using energy-dispersive X-ray spectroscopy (EDS) attached to a scanning electron microscope (SEM, Hitachi SU8010). XPS depth profiling was carried out on a Thermo Scientific K-Alpha spectrometer using cluster ion etching (Ar_{1500}^+). Fourier transform infrared (FTIR) spectra were recorded on a Nicolet iS50 spectrometer in the range of 400–4000 cm^{-1} using the KBr pellet method. The magnetic properties were measured at room temperature using a vibrating sample magnetometer (VSM, Lake Shore 7404) with an applied field ranging from −20 000 to 20 000 Oe.

Batch adsorption experiments

Prepare a phosphate stock solution with a concentration of 100 mg P per L in a volumetric flask using KH_2PO_4. First, investigate the effect of pH on phosphate adsorption over a pH range of 3.0–9.0 at 2.0 pH intervals. Adjust the pH of the solution by adding 0.1 M HCl or NaOH. Add 10 mg of adsorbent to 50 mL of solution containing 100 mg P per L phosphate and then place the conical flask in a thermostatic shaker, agitating at 200 rpm for 120 min. After equilibrium is reached, separate the solid from the aqueous suspension using magnetic separation, and determine the residual phosphate concentration in the solution at a wavelength of 820 nm using a microplate reader (SpectraMax M2) according to standard procedures. The adsorption capacity is calculated using the following formula:

$$q_e = \frac{(C_0 - C_e) \times V}{m} \quad (1)$$

where C_0 and C_e (mg P per L) are the initial and equilibrium phosphate concentrations, respectively; V (L) is the volume of the solution; and m (g) is the mass of the adsorbent used. All experiments were performed in duplicate, and average values are reported.

Aquatic toxicity assessment

Chlorella sp. was selected as the model organism to evaluate the potential environmental impact of 2.5%La-Fe_3O_4@PDA. Algal cells in the logarithmic growth phase were inoculated into fresh culture medium to achieve an initial optical density (OD) of 0.16 at 680 nm. The 2.5%La-Fe_3O_4@PDA stock solution was then added to the algal suspensions to obtain final material concentrations of 0 (control), 20, 40, 80, 100, and 200 mg L^{-1}. The exposure period lasted for 30 days, with sampling conducted every 5 days.

To monitor algal growth, the optical density of the *Chlorella* sp. suspension was measured using a UV-Vis spectrophotometer. A full-wavelength scan from 350 to 800 nm was first performed to determine the maximum absorption wavelength, which was identified as 680 nm. Subsequently, at each sampling time point (every 5 days), the absorbance at 680 nm (OD_{680}) was recorded. All experiments were performed in triplicate, and the results were expressed as mean ± standard deviation (SD).

Results and discussion

Characterization of the La-Fe_3O_4@PDA composite

Morphology and TEM analysis. The morphology and microstructure of the samples were observed by transmission electron microscopy (TEM). The pure Fe_3O_4 nanoparticles are mainly spherical, with an average diameter of approximately 200 nm (Fig. 1a). After doping with La (Fig. 1b), the La-Fe_3O_4 particles maintain a similar spherical morphology, but with a slightly increased diameter and improved monodispersity, indicating that La was successfully incorporated without significant aggregation. The La-Fe_3O_4@PDA composite exhibits a distinct core–shell structure (Fig. 1c). The darker La-Fe_3O_4 core is uniformly coated with a PDA shell, with a shell thickness of approximately 50 nm. Some degree of aggregation is observed between the particles, which may be due to magnetic interactions and hydrogen bonding between the PDA coatings.

XRD analysis. The crystal structures of Fe_3O_4, La-Fe_3O_4, and La-Fe_3O_4@PDA nanoparticles were characterized using XRD (Fig. 1d). The diffraction peaks of Fe_3O_4 (30.1°, 35.5°, *etc.*) are consistent with the standard XRD pattern (ICDD 01-073-0689).[36] After La doping, the crystal structure of La-Fe_3O_4 remained unchanged, with a slight increase in peak intensity. This observation is consistent with the successful incorporation of La into the Fe_3O_4 particles and may contribute to improved crystallinity. After further coating with a PDA layer, the diffraction peak patterns of La-Fe_3O_4@PDA are basically consistent with those of La-Fe_3O_4, showing sharper peak shapes and the highest intensity. These results suggest that the PDA coating does not disrupt the structural integrity of the Fe_3O_4 core.

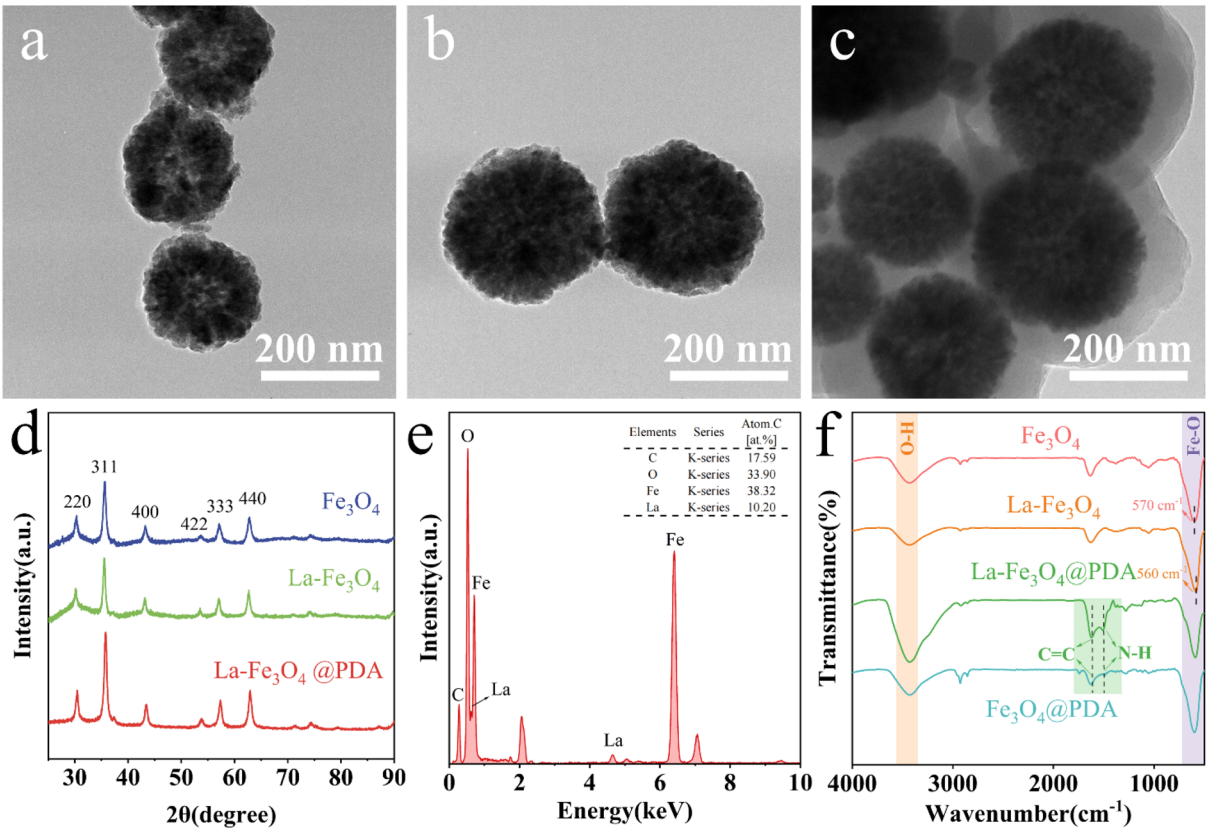

Fig. 1 TEM images of (a) Fe_3O_4, (b) La-Fe_3O_4 and (c) La-Fe_3O_4@PDA. (d) XRD patterns. (e) Elemental analysis of La-Fe_3O_4. (f) FT-IR spectra.

Together with the La-Fe_3O_4 core, the composite exhibits enhanced crystallinity.

Composition and bulk distribution analysis. The elemental composition of the prepared samples was preliminarily examined by energy-dispersive X-ray spectroscopy (EDS). The corresponding EDS spectra (Fig. 1e and S1) confirmed the coexistence of Fe, O, and La, indicating that lanthanum had been successfully introduced into the material. However, in order to rigorously determine whether La was uniformly incorporated throughout the Fe_3O_4 particles rather than merely existing as a surface adsorbate, X-ray photoelectron spectroscopy (XPS) combined with *in situ* cluster ion etching was performed. Depth profiling was conducted on La-Fe_3O_4 particles (with an average size of approximately 250 nm) at etching depths of 0 nm (surface), 30 nm, and 60 nm.

As summarized in Table S1, the surface La/Fe atomic ratio is 1.92%. At depths of 30 nm (1.15%) and 60 nm (1.49%), the La/Fe atomic ratios remain essentially constant within the typical experimental uncertainty of XPS quantification, and are both significantly lower than the surface value (1.92%). This trend indicates a slight surface segregation feature, which is a common phenomenon in transition metal oxide systems. Subsequently, La exhibits a uniform distribution throughout the particles. In addition, the normalized high-resolution La 3d and Fe 2p spectra (Fig. S2) show consistent peak shapes and binding energies at different etching depths, further confirming that La and Fe maintain similar chemical coordination environments from the surface to the bulk. Overall, the constant La/Fe ratio and superimposable La 3d and Fe 2p spectra across etching depths strongly support homogeneous incorporation of La rather than discrete surface phases.

FTIR analysis. FTIR spectroscopy was used to investigate the chemical structures and surface functional groups (Fig. 1f). All samples show a broad, strong absorption band around 3390 cm^{-1} and a medium band at ~1630 cm^{-1}, assigned to the O–H stretching vibration of surface-adsorbed water/hydroxyl groups and the H–O–H bending vibration, respectively, indicating the hydrophilic nature of the materials.

In the range of 500–600 cm^{-1}, the peak at ~570 cm^{-1} corresponds to the expansion and contraction of the tetrahedral Fe–O bond. For La-Fe_3O_4 samples, the Fe–O characteristic peaks are redshifted to about ~560 cm^{-1}, and the peak shape is slightly widened. This change can be attributed to the incorporation of larger-radius La^{3+} (≈1.06 Å) into the Fe_3O_4 particles, which leads to local structural distortion and a reduction in local symmetry, thereby decreasing the force constant of the Fe–O bond.[37]

For samples coated with polydopamine (PDA), both Fe_3O_4@PDA and La-Fe_3O_4@PDA exhibit a pair of clear absorption peaks at ~1610 cm^{-1} and 1510 cm^{-1}, corresponding to the C=C skeleton vibration and the NH surface of the aromatic ring in PDA, respectively. Bending vibration, which confirms that the PDA shell layer is successfully covered on the surface of both types of core materials. La-Fe_3O_4@PDA has a slightly strong absorption peak and displacement at ~1280 cm^{-1} (C–O

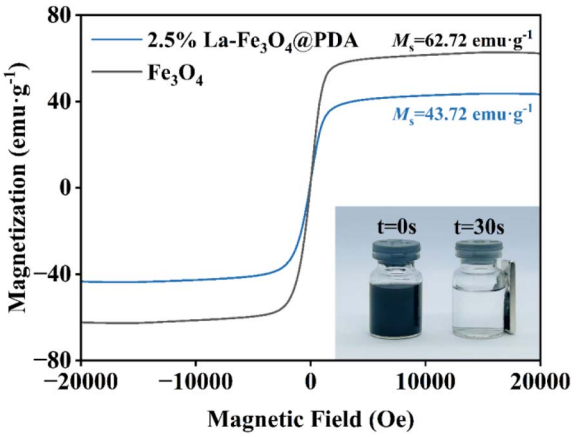

Fig. 2 Magnetization curves of Fe_3O_4 and 2.5%La-Fe_3O_4@PDA nanoparticles at room temperature.

expansion vibration), and the O–H wide peak at ~3400 cm^{-1} is also more significant. These changes may be attributed to the coordination of La^{3+} with phenol hydroxyl groups, amino groups, and other functional groups in the PDA shell, resulting in La–O–C coordinated bonds (Fig. S3). This indicates that the modification not only affects the Fe_3O_4 kernel but also regulates the chemical environment of the PDA shell interface.

VSM analysis. Magnetic properties of Fe_3O_4 and 2.5%La-Fe_3O_4@PDA were investigated using a vibrating sample magnetometer (VSM) at room temperature. Fig. 2 shows the magnetic hysteresis loops of both samples. The saturation magnetization (M_s) of 2.5%La-Fe_3O_4@PDA was determined to be 43.72 emu g^{-1}, which is lower than that of pristine Fe_3O_4 (62.72 emu g^{-1}). This decrease is attributed to the incorporation of La^{3+} ions and the coating of polydopamine (PDA) on the surface, both of which introduce non-magnetic components. Importantly, the remanent magnetization (M_r) and coercivity (H_c) of 2.5%La-Fe_3O_4@PDA are only 2.18 emu g^{-1} and 67.37 Oe (Table S2), respectively, indicating soft ferromagnetic behavior that facilitates easy redispersion after removal of the external magnetic field. Despite the reduced saturation magnetization, the value remains well above the typical threshold required for effective magnetic separation (>10 emu g^{-1}).[38] As demonstrated in the photograph inset of Fig. 2, the 2.5%La-Fe_3O_4@PDA

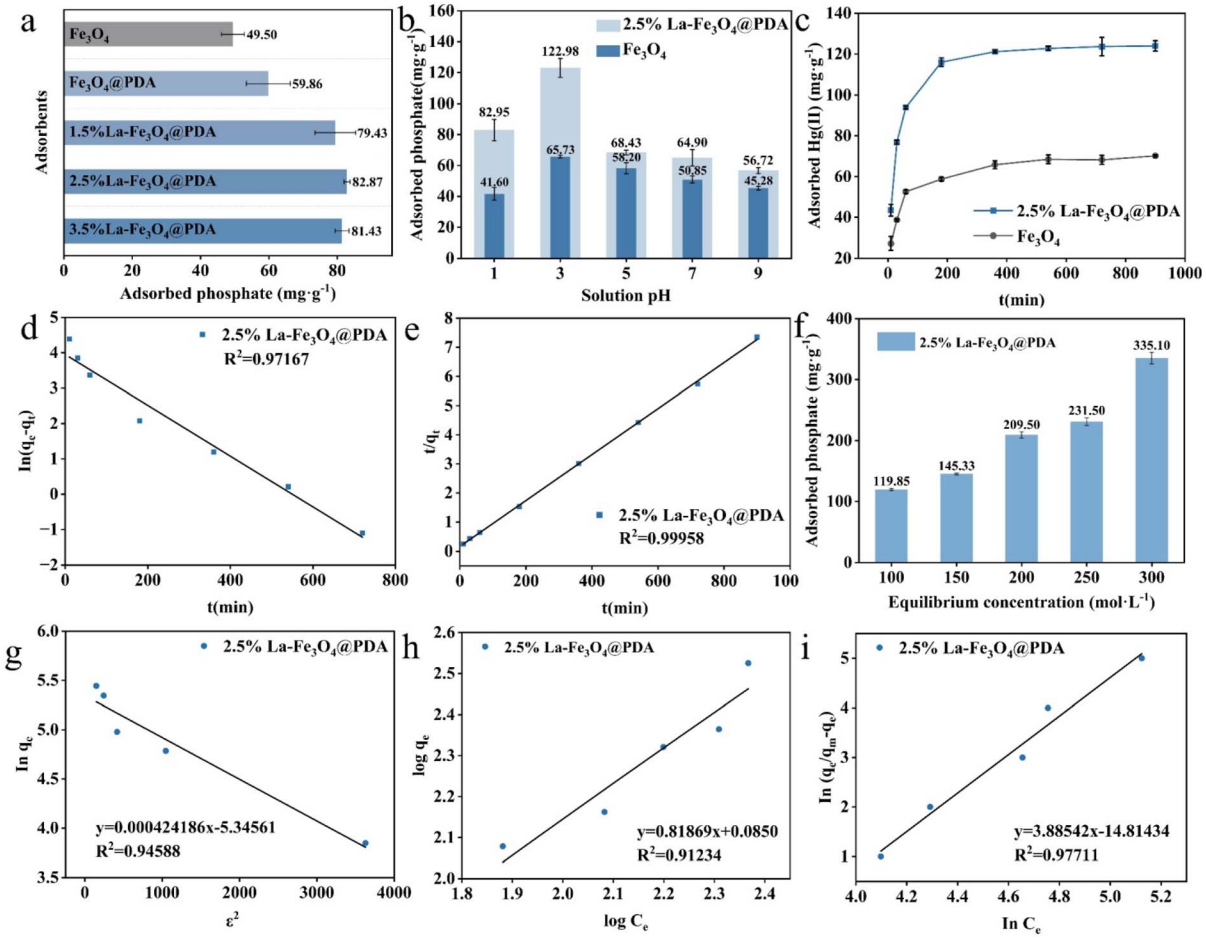

Fig. 3 (a) Phosphate adsorption performance of Fe_3O_4, Fe_3O_4@PDA, and Fe_3O_4@PDA with different La loading amounts. (b) Effect of pH on the phosphate adsorption performance of 2.5%La-Fe_3O_4@PDA and Fe_3O_4. (c) Effect of contact time on phosphate adsorption capacity of Fe_3O_4 and 2.5%La-Fe_3O_4@PDA. (d) Pseudo-first-order kinetic fitting for phosphate adsorption. (e) Pseudo-second-order kinetic fitting for phosphate adsorption. (f) Effect of initial phosphate concentration on adsorption capacity. (g) Dubinin–Radushkevich (D–R) isotherm model fitting. (h) Freundlich isotherm model fitting. (i) Sips isotherm model fitting. *Data are shown as mean ± SD ($n = 3$) for all panels.

particles can be completely attracted to a conventional magnet within 30 s. These results confirm that the material possesses sufficiently strong magnetism for rapid and efficient separation from aqueous solutions, supporting its practical application in wastewater treatment.

Adsorption performance of La-Fe_3O_4@PDA

Effect of La doping concentration. La doping plays a crucial role in enhancing the phosphate capture capacity of Fe_3O_4-based adsorbents, as the introduction of La^{3+} provides high-affinity sites that specifically bind to phosphate ions. To systematically investigate the effect of La doping concentration on adsorption behavior, this study prepared Fe_3O_4@PDA composites with varying La doping ratios, using Fe_3O_4@PDA and pure Fe_3O_4 as control samples (Fig. 3a). Among them, the 2.5%La-Fe_3O_4@PDA material exhibited the optimal adsorption capacity, reaching 82.87 mg P per g. Compared to pure Fe_3O_4 (49.50 mg P per g), this represents an increase of approximately 67.3%; relative to Fe_3O_4@PDA (59.86 mg P per g), it also reflects an enhancement of 38.4%. These data indicate a significant synergistic promotion effect between La doping and the PDA coating. As a functional carrier, PDA not only contributes to a large number of surface functional groups but also provides anchoring sites for La^{3+}. On the other hand, the introduction of La^{3+} further strengthens the material's selective recognition and binding ability toward phosphate ions.

When the La doping ratio is further increased from 2.5% to 3.5%, the phosphate adsorption capacity of the material declines slightly. This may be due to excessively high La^{3+} content covering some active sites or even causing aggregation, resulting in a reduction of the material's effective specific surface area and the availability of active sites. Pure Fe_3O_4 exhibits the lowest adsorption capacity, which is attributed to the lack of effective surface functional group modifications and the tendency of magnetic particles to aggregate, significantly limiting the available adsorption sites. PDA coating treatment brings about a notable improvement. This polymer layer not only introduces abundant nitrogen- and oxygen-containing functional groups, thereby enhancing the surface complexation capability, but also improves the overall stability of the material. Moderate La doping, based on the advantages conferred by the PDA layer, further optimizes the chemical properties of the material surface and enhances its affinity for phosphate.

Therefore, La doping combined with PDA modification exhibits a clear synergistic effect in enhancing the adsorption performance of Fe_3O_4, jointly optimizing the surface properties and composition of adsorption sites of the material. Among them, a 2.5%La doping ratio demonstrates the best phosphate adsorption performance in this system; thus, this doping ratio was selected for further in-depth study in the subsequent experiments.

Effect of initial pH. The pH of the aqueous environment plays a crucial role in the phosphate adsorption process, as it simultaneously affects both the surface charge of the adsorbent and the speciation of phosphate ions. Within the pH range of 1.0–9.0, the adsorption performance of 2.5%La-Fe_3O_4@PDA and pure Fe_3O_4 for phosphate was evaluated (Fig. 3b). The results indicate that under all tested pH conditions, the adsorption capacity of 2.5%La-Fe_3O_4@PDA was significantly higher than that of pure Fe_3O_4, primarily due to the synergistic effect of La doping and PDA coating, which provides the material with a richer set of surface functional groups and a more optimized pore structure. At pH 3.0, 2.5%La-Fe_3O_4@PDA exhibited the highest adsorption capacity, reaching 122.98 mg P per g, approximately 87.1% higher than pure Fe_3O_4 (65.73 mg P per g).

It can also be observed from the figure that as the pH value continues to increase from 3.0, the adsorption capacities of both materials show a gradual decreasing trend. Even under alkaline conditions (pH 9.0), 2.5%La-Fe_3O_4@PDA still maintains an adsorption capacity of 56.72 mg P per g, which is approximately 25.2% higher than that of unmodified Fe_3O_4, indicating that La doping effectively broadens the operational pH window of the material. Although the maximum adsorption capacity is achieved at pH 3.0 in controlled deionized water systems, the material retains substantial phosphate removal performance under near-neutral conditions commonly encountered in real wastewater. As demonstrated in spiked tap water and lake water samples (natural pH typically 6.5–8.0, initial phosphate concentration of 20 mg P per L), the removal efficiency exceeded 91% (Fig. 4f). This indicates that extensive pH adjustment may not be necessary for many practical applications, thereby enhancing the feasibility of 2.5%La-Fe_3O_4@PDA despite the acidic optimum observed under idealized batch conditions. Nevertheless, for applications requiring maximum capacity, mild acidification could be considered as a trade-off. Based on the above findings, subsequent adsorption experiments in simulated solutions were conducted at pH 3.0 to fully exploit the maximum adsorption potential of the material.

Effect of contact time and adsorption kinetics. Adsorption time is a key factor affecting the performance of adsorbents. The effect of adsorption time on the adsorption capacity of the adsorbents (2.5%La-Fe_3O_4@PDA and Fe_3O_4) is illustrated (Fig. 3c). The adsorption capacities of Fe_3O_4 and 2.5%La-Fe_3O_4@PDA for phosphate increase with time and gradually level off after a certain period. Both adsorbents exhibit a faster adsorption rate within the first 60 min, after which the rate begins to stabilize. Fe_3O_4 and 2.5%La-Fe_3O_4@PDA reach adsorption equilibrium at 360 min and 180 min, respectively. This is because, at the initial stage of adsorption, the concentration difference between phosphate in solution and the adsorbent surface drives the rapid migration of phosphate ions to the adsorbent surface. Meanwhile, a large number of active adsorption sites are available on the adsorbent surface, providing phosphate ions in the solution with more opportunities to occupy these sites. As adsorption time increases, these active sites become primarily occupied, and the negative charges on the adsorbed anions repel phosphate ions in the water, making further adsorption more difficult. Consequently, the adsorption rate gradually decreases and eventually reaches equilibrium. Since 2.5%La-Fe_3O_4@PDA contains lanthanum sites as well as polar groups such as amino and hydroxyl groups,

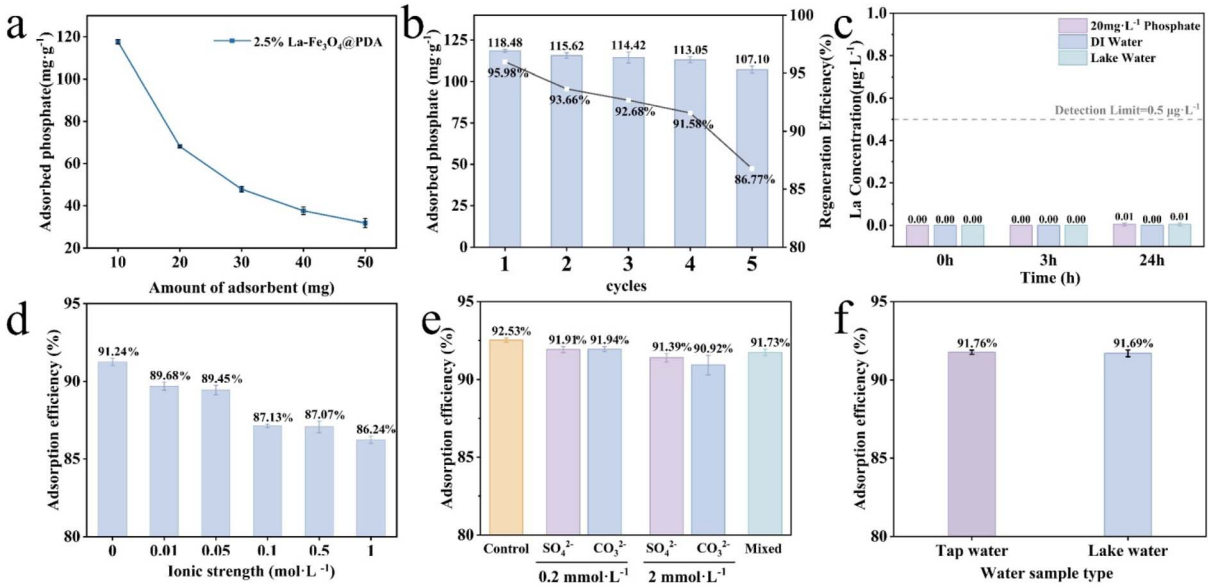

Fig. 4 (a) Effect of different adsorbent doses on the adsorption of phosphate. (b) Variation of the adsorption capacity and regeneration efficiency of 2.5%La-Fe_3O_4@PDA for phosphate with the number of adsorption–desorption cycles. (c) Comparison of La leaching behavior from 2.5%La-Fe_3O_4@PDA under various conditions. (d) Effect of ionic strength on phosphate adsorption by 2.5%La-Fe_3O_4@PDA (initial phosphate concentration: 20 mg P per L). (e) Effect of coexisting anions on phosphate adsorption by 2.5%La-Fe_3O_4@PDA (initial phosphate concentration: 20 mg P per L). (f) Adsorption capacity of 2.5%La-Fe_3O_4@PDA phosphate in different media.

its affinity and selectivity for phosphate are higher than those of Fe_3O_4, facilitating the interaction between phosphate ions and the adsorbent surface. Therefore, the equilibrium time for 2.5% La-Fe_3O_4@PDA is shorter.

$$\ln(q_e - q_t) = \ln q_e - k_1 t \quad (2)$$

$$\frac{t}{q_t} = \frac{1}{k_2 {q_e}^2} + \frac{t}{q_e} \quad (3)$$

A linear relationship between $\ln(q_e - q_t)$ and t was observed at different initial phosphate concentrations (Fig. 3d). The plot was obtained by further analyzing q_t *versus* t using the pseudo-second-order rate law (Fig. 3e). The parameters for the pseudo-first order and pseudo-second-order kinetics were determined from the slopes and intercepts of the respective curves.[8] The correlation coefficient of the pseudo-second-order kinetic model ($R^2 = 0.99958$) is higher than that of the pseudo-first-order kinetic model ($R^2 = 0.97167$) (Table S3).

Therefore, the adsorption kinetics of 2.5%La-Fe_3O_4@PDA follow a pseudo-second-order model, indicating that the adsorption of phosphate by 2.5%La-Fe_3O_4@PDA may be consistent with chemisorption; that is, electrons are shared or exchanged between the adsorbent and the adsorbate, and phosphate ions are adsorbed through the formation of coordination bonds or ion exchange.

Adsorption isotherms and mechanism. To investigate the adsorption mechanism and surface properties of 2.5%La-Fe_3O_4@PDA toward phosphates, this study measured its adsorption performance within a phosphate concentration range of 100 to 300 mg P per L (Fig. 3f). The adsorption capacity (q_e) continuously increased with rising phosphate concentrations. This indicates that higher concentrations provide a greater mass transfer driving force, allowing phosphate ions to fully interact with the abundant active sites on the material's surface. To gain a deeper understanding of the adsorption mechanism, the Dubinin–Radushkevich (D–R), the Freundlich, and the Sips isotherm models were used to describe the adsorption equilibrium of 2.5%La-Fe_3O_4@PDA (Fig. 3g–i). These isotherm equations can be expressed as follows:

$$\ln q_e = \ln q_d - K_d \varepsilon^2 \quad (4)$$

$$\log q_e = \log k + \frac{1}{n} \log C_e \quad (5)$$

$$\ln\left(\frac{q_e}{q_m - q_e}\right) = \beta \ln b + \beta \ln C_e \quad (6)$$

Among them, q_e (mg P per g) and q_d (mol g^{-1}) are the adsorption capacity at equilibrium and the maximum adsorption capacity, respectively; K_d (mol^2 kJ^{-2}) is a constant related to adsorption energy; ε is the Polanyi potential ($\varepsilon = RT\ln(1 + {C_e}^{-1})$, C_e (mg P per L) is the phosphate concentration at equilibrium); K [(mol g^{-1}) (mol $L^{-1})^{-1/n}$] can be regarded as the adsorption amount per unit concentration of phosphate; $1/n$ is an indicator of adsorption intensity. q_m is the maximum adsorption capacity (mg P per g); β is an indicator of adsorption strength; b [L per mg P] is the Sips equilibrium constant.

In addition, equilibrium parameters RL = $(1 + bC_0)^{-1}$, the highest initial solute concentration in the concentration gradient C_0 (mg P per L), and the mean free energy of adsorption $E_d[(2K_d)^{-1/2}$, kJ mol^{-1}] were also estimated.

The fitted correlation coefficients indicate that the Sips model has the highest correlation coefficient ($R^2 = 0.977$), outperforming the D–R model ($R^2 = 0.945$) and the Freundlich model ($R^2 = 0.912$) (Table S4). The Sips model, a combination of the Langmuir and Freundlich models, suggests that the adsorption process exhibits both a tendency toward monolayer adsorption and characteristics of a heterogeneous surface. This is highly consistent with the material design: La^{3+} sites with high surface affinity contribute to monolayer adsorption, while polydopamine (PDA) functional groups with a broader energy distribution contribute to heterogeneous adsorption behavior, synergistically forming a composite adsorption interface.

The Freundlich model also demonstrates a good fit, further confirming the heterogeneity of the adsorbent surface, which aligns with the disordered structure of the PDA layer and the uneven energy distribution of active sites. Its parameter $n > 1$ indicates a strong affinity between phosphate and the adsorbent, making the adsorption process favorable. Based on the D–R model, the average adsorption free energy (E) was calculated to be 34.32 kJ mol^{-1}. This value falls within the range of 20–40 kJ mol^{-1},[39] indicating that the adsorption process is primarily governed by chemisorption, consistent with the potential formation of inner-sphere complexes between La^{3+} and PO_4^{3-}.

To further investigate the proposed chemisorption mechanism, X-ray photoelectron spectroscopy (XPS) was performed on the material before and after phosphate adsorption. As shown in Table S5, the La $3d_{5/2}$ binding energy shifted from 835.1 eV to 835.6 eV after phosphate adsorption, accompanied by an increase in the satellite-to-main peak intensity ratio (from 0.44 to 0.51). These spectral changes are characteristic of the formation of a La–O–P inner-sphere complex, as previously reported for $LaPO_4$ and related La-based adsorbents. The Fe 2p binding energy remained unchanged after adsorption, ruling out direct Fe participation in phosphate binding. The P 2p signal approaches the detection limit, but a weak peak is still observed at approximately 133.6 eV, which is higher than that of free phosphate ($\approx$133.2 eV) and is consistent with La–O–P coordination.[40] Collectively, these XPS results (shift in La $3d_{5/2}$ binding energy and increased satellite intensity, together with a weak P 2p signal at $\sim$133.6 eV) are consistent with the formation of inner-sphere La–O–P complexes. Although the P 2p signal intensity is low, the observed spectral changes align with literature reports on La-phosphate interactions and support the chemisorption mechanism inferred from the D–R model ($E = 34.32$ kJ mol^{-1}).

Effect of adsorbent dose and performance comparison. Fig. 4a shows the effect of different adsorbent dosages (10–50 mg) on phosphate adsorption. The adsorption capacity of phosphate gradually decreases with the increase of the adsorbent dosage. Under conditions where the initial phosphate concentration and solution volume remain constant, increasing the adsorbent dosage provides more theoretically active sites for adsorption to occur. However, the number of phosphate ions adsorbed per unit mass of adsorbent correspondingly decreases, leading to incomplete saturation of active sites. In addition, higher adsorbent concentrations may cause aggregation between particles, reducing the effective specific surface area and the effective utilization of active sites, further limiting the increase in adsorption capacity.

Regeneration efficiency of La-Fe_3O_4@PDA. The stability and recyclability of adsorbents during multiple adsorption–desorption cycles are crucial for improving the cost-effectiveness of the adsorption process. In this study, a 1 M NaCl solution was selected as the eluent for the regeneration process. Fig. 4b shows the phosphate adsorption performance during adsorption–desorption cycles. Although the phosphate adsorption capacity of 2.5%La-Fe_3O_4@PDA gradually decreased with increasing adsorption–desorption cycles, the regeneration efficiency reached 86.77% after five cycles.

The adsorption performance of 2.5%La-Fe_3O_4@PDA was compared with previously reported phosphate adsorbents (Table S6). Although the equilibrium time of 180 min is not the shortest among the compared materials, it is comparable to or even shorter than that of many conventional adsorbents, which often require equilibrium times of 600–1440 min.[41,42] The adsorption capacity of 123.44 mg P per g is among the higher values reported for similar materials, indicating that the present adsorbent exhibits competitive phosphate uptake capability. In addition to adsorption performance, the material offers practical advantages such as magnetic recoverability, environmental safety, and satisfactory reusability, and low cost of regeneration (using NaCl as the eluent), making it a promising candidate for phosphate removal applications.

To further evaluate the stability of the material during the regeneration process, the potential leaching of La was investigated under different conditions. The 2.5%La-Fe_3O_4@PDA was immersed in three different media (20 mg P per L phosphate solution, deionized water, and lake water), and La concentrations in the supernatant were measured by ICP-MS at 0 h, 3 h, and 24 h. As shown in Fig. 4c, La was below the detection limit in deionized water at all time points. In phosphate solution and lake water, La remained below the detection limit at 0 h and 3 h, while a concentration of only 0.01 μg L^{-1} was detected at 24 h, a value well below the detection limit and considered negligible. These results confirm that La is stably and homogeneously incorporated throughout the Fe_3O_4 particles and does not leach into the aqueous phase during the adsorption and regeneration processes, further supporting the excellent stability and reusability of the material.

Effect of water matrix conditions on phosphate adsorption. To evaluate the robustness of 2.5%La-Fe_3O_4@PDA under various water matrix conditions, the effects of ionic strength, coexisting anions, and real water matrices were systematically investigated.

The influence of ionic strength on phosphate adsorption was examined using NaCl as the background electrolyte at concentrations ranging from 0 to 1.0 mol L^{-1}. As shown in Fig. 4d, the phosphate removal efficiency gradually decreased with increasing ionic strength. In the absence of NaCl (control), the removal efficiency was 91.24%. At NaCl concentrations of 0.01 and 0.05 mol L^{-1}, the efficiencies slightly decreased to 89.68% and 89.45%, respectively. Further increases to 0.1, 0.5, and 1.0 mol L^{-1} resulted in removal efficiencies of 87.13%, 87.07%,

and 86.24%, respectively. The moderate decrease in adsorption efficiency with increasing ionic strength suggests that electrostatic interactions contribute to phosphate adsorption, but the material retains a high removal capacity (>86%) even under high ionic strength. This behavior is consistent with an inner-sphere complexation mechanism, wherein specific chemical bonding between La^{3+} and phosphate is the dominant driving force.

The selectivity of 2.5%La-Fe_3O_4@PDA toward phosphate was assessed in the presence of common competing anions, SO_4^{2-} and CO_3^{2-}, at concentrations of 0.2 and 2.0 mmol L^{-1}. A mixed solution containing both anions (each at 1.0 mmol L^{-1}) was also tested. The initial phosphate concentration was fixed at 20 mg P per L. As shown in Fig. 4e, the control (without competing anions) achieved a removal efficiency of 92.53%. In the presence of 0.2 mmol L^{-1} SO_4^{2-} or CO_3^{2-}, the efficiencies were 91.91% and 91.94%, respectively. At the higher concentration of 2.0 mmol L^{-1}, the removal efficiencies remained above 90%. The mixed anion system gave a removal efficiency of 91.73%. These results demonstrate that coexisting anions do not significantly interfere with phosphate adsorption, confirming the excellent selectivity of the material. This high selectivity is also attributed to the strong affinity of La^{3+} sites for phosphate *via* inner-sphere complexation.

To further evaluate the practical applicability of 2.5%La-Fe_3O_4@PDA, the standard addition method was used to test tap water and lake water (collected from Shihezi City). Both water samples were filtered through 0.22 μm membrane filters to remove suspended solids. The initial phosphate concentrations in the raw samples were negligible. Therefore, phosphate standard solution was spiked into each sample to achieve an initial phosphate concentration of 20 mg P per L. Subsequently, 10 mg of 2.5%La-Fe_3O_4@PDA was added to 50 mL of each spiked water sample. As shown in Fig. 4f, the phosphate removal efficiencies in tap water and lake water were 91.76% and 91.69%, respectively, which are comparable to those obtained in deionized water (92.53%). These results demonstrate that the material remains highly effective under near-neutral pH conditions (the natural pH of the tested waters), even though the maximum adsorption capacity is observed at pH 3.0 in controlled laboratory experiments. Thus, the presence of natural organic matter and co-existing ions does not significantly impair performance, confirming the feasibility of 2.5% La-Fe_3O_4@PDA for practical phosphate removal applications.

Taken together, the material exhibits stable and efficient phosphate adsorption across a wide range of water matrix conditions, including high ionic strength, the presence of competing anions, and real natural water samples. These findings further support that phosphate uptake proceeds primarily through an inner-sphere complexation mechanism, and underscore the potential of 2.5%La-Fe_3O_4@PDA as a robust adsorbent for real-world wastewater treatment.

Aquatic toxicity of 2.5%La-Fe_3O_4@PDA toward *Chlorella* sp.. To evaluate the potential environmental impact of 2.5%La-Fe_3O_4@PDA, the growth of *Chlorella* sp. was monitored over 30 days in the presence of 0–200 mg L^{-1} of the material. As shown in Fig. 5, the optical density (OD_{680}) of all groups increased steadily from day 0 to day 30, indicating continuous algal growth across all tested concentrations.

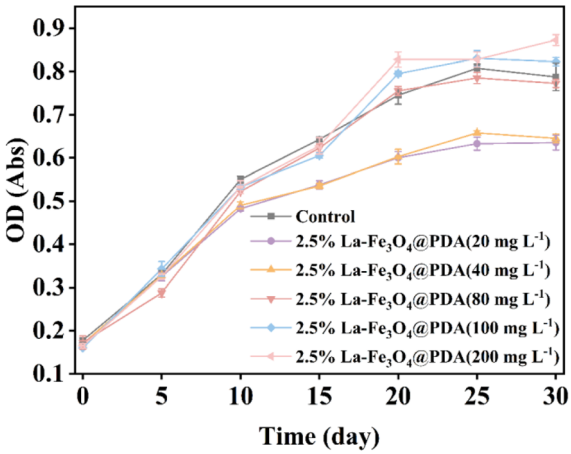

Fig. 5 Effect of different 2.5%La-Fe_3O_4@PDA concentrations on the OD of *Chlorella* sp.

Notably, at higher concentrations (100 and 200 mg L^{-1}), the final OD_{680} values were comparable to, or even slightly higher than, those of the control group (0.8225 and 0.8725 *vs.* 0.7875). This observation suggests that the material does not exert acute toxicity toward *Chlorella* sp. within the tested concentration range. The slightly lower OD values observed at low concentrations (20 and 40 mg L^{-1}) may be attributed to physical effects such as light scattering or shading caused by well-dispersed particles in the culture medium, rather than chemical toxicity. At higher concentrations (100 and 200 mg L^{-1}), the particles tend to aggregate and settle, reducing light interference and allowing more efficient algal growth. This interpretation is strongly supported by the negligible La leaching (<0.01 μg L^{-1}) confirmed by ICP-MS analysis, which rules out the possibility of toxic metal ion release. Furthermore, scanning electron microscopy (SEM) images of *Chlorella* sp. after 30 days of exposure (Fig. S4) showed intact cell morphology with no visible surface damage, cracking, or lysis across all tested concentrations, further confirming the absence of acute toxic effects.

Cost and scalability considerations

To assess the practical potential of 2.5%La-Fe_3O_4@PDA, we estimated the raw material cost based on current market prices (Table S7). The composite was synthesized *via* a simple one-pot hydrothermal method (200 °C, 10 h) followed by room-temperature PDA coating. The estimated raw material cost is approximately 0.04–0.05 USD per g when excluding the recoverable solvent (ethylene glycol). Magnetic separation eliminates the need for energy-intensive centrifugation or filtration, significantly reducing operational costs compared with non-magnetic nano-adsorbents. The use of 1 M NaCl as a low-cost regenerant further enhances economic viability.

From a scalability perspective, hydrothermal synthesis is industrially mature. Future optimization may include continuous-flow hydrothermal reactors and more cost-effective dopamine

analogs (*e.g.*, tannic acid) to further lower costs. Although the raw material cost (≈40 USD per kg) is higher than that of some commercial adsorbents (*e.g.*, activated alumina or lanthanum-modified resins, typically $5–20 per kg),[25] the high reusability (>85% capacity retention after five cycles) reduces the effective cost per cycle to approximately 8 USD per kg, making the material economically competitive on a life-cycle basis. Overall, these attributes position 2.5%La-Fe_3O_4@PDA as a cost-effective and scalable option for large-scale wastewater treatment.

Conclusions

In this study, a La-doped Fe_3O_4@PDA core–shell composite was fabricated and comprehensively evaluated as a high-performance phosphate adsorbent, with emphasis on mechanistic validation of uniform La incorporation into the Fe_3O_4 matrix and inner-sphere La–P complexation. XPS depth profiling confirmed that La is uniformly distributed throughout the Fe_3O_4 particles rather than merely present on the surface, with a constant La/Fe ratio from the surface to 60 nm depth. The optimized material, 2.5%La-Fe_3O_4@PDA, exhibited excellent phosphate adsorption capacity (123.44 mg P per g) and rapid equilibrium (180 min), following pseudo-second-order kinetics and the Sips isotherm model. XPS analysis revealed shifts in the La 3d spectra consistent with the formation of inner-sphere La–P complexes, further supporting the chemisorption mechanism. The adsorbent retained over 85% of its initial capacity after five consecutive adsorption–desorption cycles using 1 M NaCl as the eluent, demonstrating excellent reusability. Although the maximum adsorption capacity was observed at pH 3.0 in controlled laboratory experiments, the material maintained high removal efficiency (>91%) in spiked real water samples at their natural near-neutral pH, indicating its potential practical applicability without extensive pH adjustment. Moreover, the material showed negligible La leaching (<0.01 μg L^{-1}) and low aquatic toxicity toward *Chlorella* sp., supporting its environmental safety. This study provides a high-performance, magnetically separable, and reusable material solution for phosphate removal from wastewater.

Author contributions

All authors have accepted responsibility for the entire content of this manuscript and approved its submission.

Conflicts of interest

There are no conflicts to declare.

Data availability

All data that support the findings of this study are included within the article.

Supplementary information (SI): Tables S1–S7 and Fig. S1–S4, covering XPS depth profiling, magnetic properties, adsorption kinetics and isotherms, binding energy changes, adsorbent comparison, material cost, elemental mapping, FT-IR, and SEM images of *Chlorella* sp. See DOI: https://doi.org/10.1039/d6ra00725b.

Acknowledgements

This work was supported by the Tianshan Elite Youth Talent Program of Xinjiang Uygur Autonomous Region (grant no. 2024TSYCJC0076) and the National Natural Science Foundation of China (grant no. 32460237).

Notes and references

1 T. L. Martinon, *RSC Sustainability*, 2023, **1**, 1594–1598.
2 M. M. Mekonnen and A. Y. Hoekstra, *Water Resour. Res.*, 2018, **54**, 345–358.
3 M. N. Nadagouda, G. Varshney, V. Varshney and C. A. Hejase, *ACS Environ. Au*, 2024, **4**, 271–291.
4 E. Zran, B. Yao, A. Trokourey, A. Yobouet and P. Drogui, *Int. J. Environ. Sci. Technol.*, 2015, **12**, 3117–3124.
5 D. Mulkerrins, A. Dobson and E. Colleran, *Environ. Int.*, 2004, **30**, 249–259.
6 A. Anwar, C. M. Rosnelly, I. Ramli, N. Arahman and A. Fahrina, *Elkawnie*, 2023, **9**, 260–274.
7 H. Bacelo, A. M. Pintor, S. C. Santos, R. A. Boaventura and C. M. Botelho, *Chem. Eng. J.*, 2020, **381**, 122566.
8 Y. Huang, X. Lee, M. Grattieri, M. Yuan, R. Cai, F. C. Macazo and S. D. Minteer, *Chem. Eng. J.*, 2020, **380**, 122375.
9 L.-g. Yan, K. Yang, R.-r. Shan, T. Yan, J. Wei, S.-j. Yu, H.-q. Yu and B. Du, *J. Colloid Interface Sci.*, 2015, **448**, 508–516.
10 M. Belaye, A. M. Taddesse, E. Teju, M. Sanchez-Sanchez and J. M. Yassin, *ACS Omega*, 2023, **8**, 23860–23869.
11 Ł. Wujcicki, T. Mańdok, W. Budzińska-Lipka, K. Pawlusińska, N. Szozda, G. Dudek, K. Piotrowski, R. Turczyn, M. Krzywiecki and A. Kazek-Kęsik, *Sci. Rep.*, 2023, **13**, 13049.
12 A. E. Angkawijaya, Y. N. Tran-Chuong, Q. N. Ha, P. L. Tran-Nguyen, S. P. Santoso, V. Bundjaja, A. W. Go, H.-Y. Hsu and Y.-H. Ju, *J. Taiwan Inst. Chem. Eng.*, 2022, **131**, 104162.
13 D. Pattappan, S. Kapoor, S. S. Islam and Y.-T. Lai, *ACS Omega*, 2023, **8**, 24727–24749.
14 C. Su, *J. Hazard Mater.*, 2017, **322**, 48–84.
15 H. Ardiyanti, E. Suharyadi, T. Kato and S. Iwata, *AIP Conf. Proc.*, 2016, **1725**, 020007.
16 S. Duan, J. Liu, Y. Pang, F. Lin, X. Meng, K. Tang and J. Li, *Molecules*, 2022, **27**, 6812.
17 S. Laurent, D. Forge, M. Port, A. Roch, C. Robic, L. Vander Elst and R. N. Muller, *Chem. Rev.*, 2008, **108**, 2064–2110.
18 Y. Li, Q. Xie, Q. Hu, C. Li, Z. Huang, X. Yang and H. Guo, *Sci. Rep.*, 2016, **6**, 30651.
19 L. Paltrinieri, M. Wang, S. Sachdeva, N. A. Besseling, E. J. Sudhölter and L. C. De Smet, *J. Mater. Chem. A*, 2017, **5**, 18476–18485.
20 H. Shen, Z. Wang, A. Zhou, J. Chen, M. Hu, X. Dong and Q. Xia, *RSC Adv.*, 2015, **5**, 22080–22090.
21 K.-W. Jung, S. Lee and Y. J. Lee, *Bioresour. Technol.*, 2017, **245**, 751–759.

22 A. I. Salim, N. A. Abdelgawad, E. Rozaik and N. G. Mostafa, *Sci. Rep.*, 2025, **15**, 24038.
23 K. Kim, D. Kim, T. Kim, B.-G. Kim, D. Ko, J. Lee, Y. Han, J. C. Jung and H. B. Na, *RSC Adv.*, 2019, **9**, 15257–15264.
24 J. Mo, Q. Li, X. Sun, H. Zhang, M. Xing, B. Dong and H. Zhu, *Water*, 2024, **16**, 418.
25 H. Wang, H. Luo, R. Han, W. Wu, J. Yang, T. Qin, L. Chen, M. Liu, B.-J. He and Z. Jing, *Sci. Rep.*, 2025, **15**, 3145.
26 Y. Zhu, X. Yue and F. Xie, *Adsorpt. Sci. Technol.*, 2020, **38**, 254–270.
27 Y. Lu, X. Jin, X. Li, M. Liu, B. Liu, X. Zeng, J. Chen, Z. Liu, S. Yu and Y. Xu, *Polymers*, 2023, **15**, 248.
28 F. Liu, R. Jamal, T. Abdiryim and X. Liu, *Cellulose*, 2022, **29**, 8025–8064.
29 H. Hemmatpour, O. De Luca, D. Crestani, M. C. Stuart, A. Lasorsa, P. C. Van Der Wel, K. Loos, T. Giousis, V. Haddadi-Asl and P. Rudolf, *Nat. Commun.*, 2023, **14**, 664.
30 G. Siciliano, A. G. Monteduro, A. Turco, E. Primiceri, S. Rizzato, N. Depalo, M. L. Curri and G. Maruccio, *Nanomaterials*, 2022, **12**, 1145.
31 M. Saraf, P. Prateek, R. Ranjan, B. Balasubramaniam, V. K. Thakur and R. K. Gupta, *Adv. Mater. Interfaces*, 2024, **11**, 2300670.
32 S. I. A. Shah, W. Ahmad, M. Anwar, R. Shah, J. A. Khan, N. S. Shah, A. Al-Anazi and C. Han, *Appl. Catal. O: Open*, 2025, **203**, 207049.
33 F. da Silva Bruckmann, C. E. Schnorr, T. da Rosa Salles, F. B. Nunes, L. Baumann, E. I. Müller, L. F. Silva, G. L. Dotto and C. R. Bohn Rhoden, *Polymers*, 2022, **14**, 4854.
34 S. G. Divakara and B. Mahesh, *Results Eng.*, 2024, **21**, 101702.
35 E. F. Aboelfetoh, *Sci. Rep.*, 2025, **15**, 27342.
36 W. Wang, L. Zheng, F. Lu, R. Hong, M. Z. Chen and L. Zhuang, *AIP Adv.*, 2017, **7**, 056317.
37 M. Zeng, K. Thummavichai, W. Chen, G. Liu, Z. Li, X. Chen, C. Feng, Y. Li, N. Wang and Y. Zhu, *RSC Adv.*, 2021, **11**, 37246–37253.
38 C. T. Yavuz, J. Mayo, W. W. Yu, A. Prakash, J. C. Falkner, S. Yean, L. Cong, H. J. Shipley, A. Kan and M. Tomson, *Science*, 2006, **314**, 964–967.
39 S. A. Odoemelam, F. K. Onwu, S. C. Uchechukwu and M. A. Chinedu, *Am. Chem. Sci. J.*, 2015, **5**, 253–269.
40 Y. He, X. Qi, J. Li, W. Wang, J. Zhang, L. Yang, M. Xue and K. Lan, *ACS Omega*, 2024, **9**, 30826–30833.
41 W. Xiong, J. Tong, Z. Yang, G. Zeng, Y. Zhou, D. Wang, P. Song, R. Xu, C. Zhang and M. Cheng, *J. Colloid Interface Sci.*, 2017, **493**, 17–23.
42 Q. Yin, H. Ren, R. Wang and Z. Zhao, *Sci. Total Environ.*, 2018, **631**, 895–903.